Nano Research

Open Access

Research Article

Probing orbital and spin moments of electron-beam-sensitive magnetic oxides via high-energy transmission electrons

Zhixin Zeng[1,§], Xiaoxiao Fu[1]✉, Jianjun Li[1,§], Hongchu Du[2], Yu Zhuo[1], Peng Tang[1], Feiyu Chen[3], Lefeng Shi[3], Rui Wu[4], Daliang Zhang[5], and Xiaoxu Huang[1]✉

[1] *International Joint Laboratory for Light Alloys (MOE), College of Materials Science and Engineering, Chongqing University, Chongqing 400044, China*
[2] *Ernst Ruska-Centre for Microscopy and Spectroscopy with Electrons, Forschungszentrum Jülich GmbH, Jülich 52425, Germany*
[3] *National Center for Applied Mathematics in Chongqing, Chongqing Normal University, Chongqing 401331, China*
[4] *Spin-X Institute, South China University of Technology, Guangzhou 511442, China*
[5] *Multi-scale Porous Materials Center, Institute of Advanced Interdisciplinary Studies & School of Chemistry and Chemical Engineering, Chongqing University, Chongqing 400044, China*
§ *Zhixin Zeng and Jianjun Li contributed equally to this work.*

Cite this article: *Nano Research*, **2026**, *19*, 94908566. https://doi.org/10.26599/NR.2026.94908566

ABSTRACT: Magnetic oxides host rich spin-orbit-coupled phenomena central to data storage and quantum technologies, yet near-atomic quantification of their spin and orbital moments remains challenging, obscuring origins of phenomena. Electron magnetic circular dichroism (EMCD) provides a unique solution, while many oxides suffer electron-induced valence changes that corrupt spectral fidelity, imposing long-standing limitations on high-resolution moment investigation. On a widely-used yet beam-irradiation-susceptible oxide $CoFe_2O_4$, we demonstrate an EMCD methodology addressing this challenge. First, a dose strategy tailoring the dose rate was proposed to preserve spectral fidelity. Second, an optimized EMCD geometry with a joint-parameter post-processing (JPP) method and an artifact correction method was developed to overcome the conflict between oxides' low tolerance of electron dose and EMCD's intrinsic demand of high dose. An example statistical analysis demonstrated that JPP method reduced background-related error of Fe orbital-to-spin ratio from 0.18 ± 0.04 to 0.12 ± 0.01, and the correction method further improved it to 0.065 ± 0.005, in high-resolution low-dose cases. These developments enable simultaneous detection of reliable EMCD signal of Fe and Co in model $CoFe_2O_4$, indicating the potential of revealing subtle variations in magnetic microstructures. Our methodology unlocks high-resolution spin-orbit-coupling research in beam-sensitive magnetic oxides.

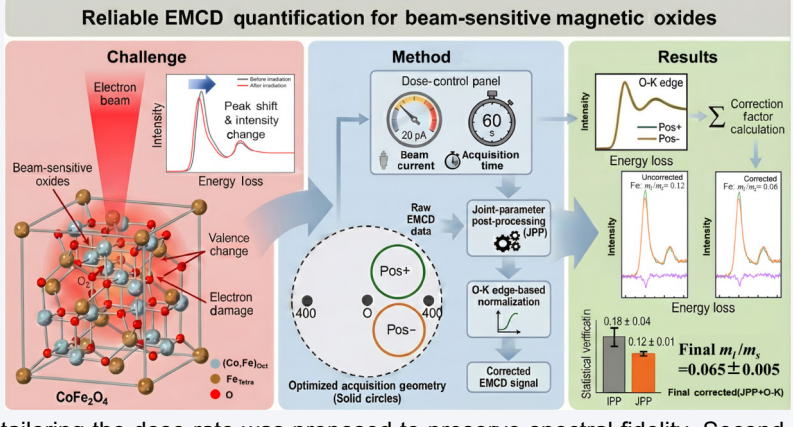

KEYWORDS: electron magnetic circular dichroism (EMCD), magnetic moment, beam sensitive, magnetic oxide

1 Introduction

Magnetic oxides have long been of great interest owing to their diverse physical phenomena and significant potential in applications such as ultra-high-density data storage, superconductivity, and quantum computing [1–3]. Understanding their spin-orbit coupling is key to unraveling the mechanisms underlying magnetic phenomena such as the spin Hall effect [4, 5], topological states [6, 7], magnetic anisotropy [8, 9], and magnetoresistance [10–12], which underpin their applications. Electron magnetic circular dichroism (EMCD), a transmission electron microscopy (TEM) technique based on momentum-resolved electron energy-loss spectroscopy (**q**-EELS), can measure

Received: January 12, 2026; **Revised:** February 10, 2026
Accepted: February 12, 2026

✉Address correspondence to Xiaoxiao Fu, xiaoxiao.fu@cqu.edu.cn; Xiaoxu Huang, xiaoxuhuang@cqu.edu.cn

spin and orbital moments at atomic resolution [13–15], thus has emerged as a powerful tool for probing spin-orbit interactions, with particular promise for investigating interfaces, defects, and topological structures.

Recently, the EMCD technique has been extensively applied to elemental metals [16–19], alloys [20–23], intermetallic compounds [24, 25], doped dilute semiconductors [26, 27], as well as oxides [28–32]. However, its efficient application to electron-beam-sensitive metal oxides remains challenging, mainly due to the intrinsic contradiction between the high electron dose demand of EMCD technique and the low dose tolerance of these oxides. On one hand, the **q**-EELS-based EMCD technique detects scattered electrons within a restricted angular range, inherently requiring high doses to resolve the weak magnetic signal from background noise. On the other hand, a large range of functional oxides, such as transition-metal or mixed-valence oxides, are susceptible to a loss of oxygen atoms and a change in valence state of metal elements under high-energy electron irradiation [33–38], which can easily distort EELS fine structures may severely undermine the reliability of the EMCD magnetic measurements, making the technique ineffective. This is more severe when EMCD experiments were performed in scanning TEM (STEM) mode for achieving high resolution. Consequently, EMCD methodologies specifically optimized for beam-sensitive oxides are highly required for achieving reliable magnetic information under strict dose limitations.

This work proposes an EMCD methodology tailored for beam-sensitive magnetic metal oxides, using a representative, widely-applied and beam-sensitive oxide $CoFe_2O_4$ as a model system. The development of the dose control strategy, the experimental configuration optimization, as well as the post-processing methods are demonstrated in detail. These efforts significantly improve the reliability of EMCD measurements of beam-sensitive oxides and open new opportunities for quantitative magnetic characterization of diverse oxide materials.

2 Results and discussion

2.1 Method design and model structure

The EMCD methodology developed in this work integrates both experimental and data-processing advances in three key aspects. First, an irradiation strategy is designed to preserve the EELS spectra shape during irradiation under optimized dose efficiency. Second, an optimized EMCD configuration, supported by a dedicated correction method, is introduced to enhance the signal-to-noise ratio (SNR) under limited doses. Finally, a post-processing approach is developed to improve the magnetic quantification precision for high-noise EMCD spectra.

The irradiation strategy is established by experimentally observing beam damage using EELS under varying cumulative doses and dose rates. In conventional on-axis EELS, beam-induced oxygen vacancies and changes in metal valence can shift peak positions and alter the shape of core-level edges, as illustrated in Figs. 1(a) and 1(b). EMCD is obtained as the difference between two consecutively acquired **q**-EELS spectra using a small off-axis aperture, as shown in Fig. 1(a). Ideally, this difference reflects only the presence of a non-zero magnetic moment. Any factor other than magnetism that brings additional differences will distort the EMCD spectrum, as displayed in Fig. 1(c), potentially introducing significant errors in the quantification of magnetic moments. Therefore, the dose needs to be restricted to preserve spectral shape, with irradiation time and spectral SNR also being important considerations.

Under a limited dose, the low SNR of EMCD spectra becomes a prominent problem. This work optimizes the EMCD configuration by placing the aperture deviating from classical positions towards diffraction spots, enabling the collection of a higher amount of inelastically scattered electrons in a single acquisition. However, this configuration can inevitably introduce artifacts into EMCD spectra due to the complex asymmetry of the intensity distribution on a diffraction plane [31, 39]. So, this work correspondingly proposed a

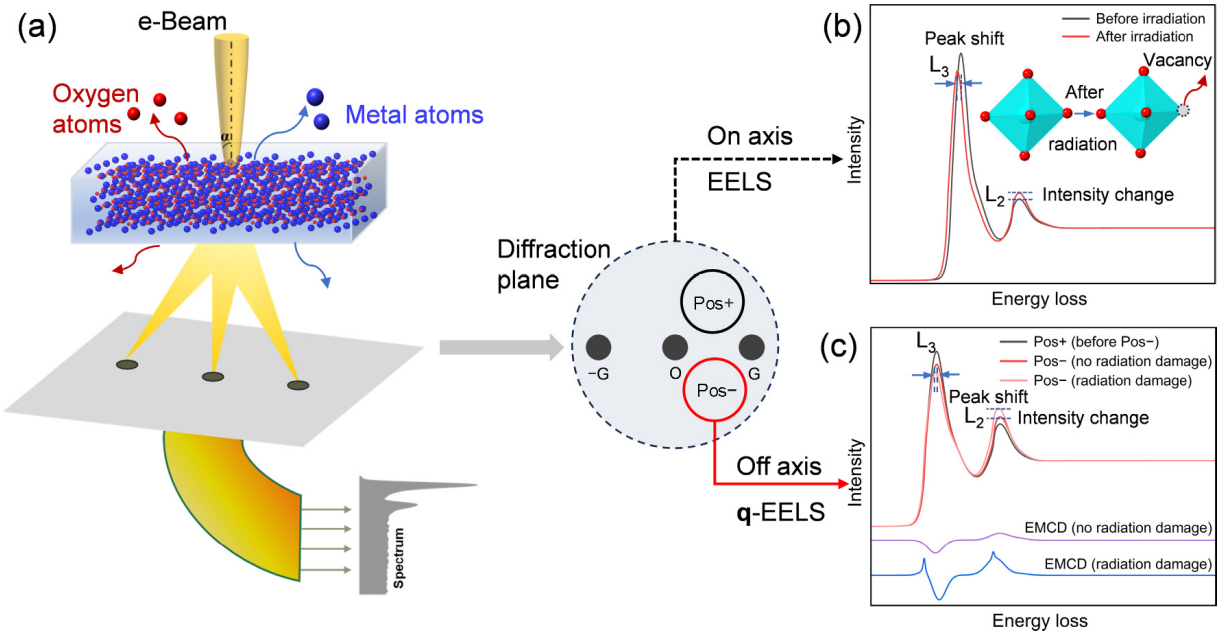

Figure 1 Schematic illustration of beam-induced change of EELS spectral shape and distortion of EMCD spectrum. (a) General EELS and EMCD experimental configuration, (b) beam-induced change of conventional on-axis core-level ionization edge, and (c) beam-induced distortion of EMCD spectra.

careful artifact removal method, referring the simulated distribution information of elastically and inelastically scattered electrons.

Despite these optimizations, EMCD spectra still exhibit higher noise levels than conventional on-axis EELS, bringing significant error to moment quantification. Consequently, a post-processing method was developed to mitigate the impact of incomplete background subtraction on quantitative accuracy in the case of limited dose conditions.

The model structure used to demonstrate the EMCD methodology is $CoFe_2O_4$ (CFO), a multi-cation spinel oxide known for its tunable ferrimagnetism, high potential for spintronic applications, and beam-sensitive high-valence cations [40–42]. Figure 2 illustrates this beam sensitivity by comparing CFO with $Y_3Fe_5O_{12}$ (YIG). Atomic-resolution high-angle annular dark-field (HAADF) STEM images of CFO ([001] zone axis) and YIG ([110] zone axis) are shown in Figs. 2(a) and 2(b) with their structure schematics in Fig. 2(c). CFO has Fe^{3+} in oxygen tetrahedra and Co^{2+}/Fe^{3+} in oxygen octahedra sites, while YIG has Y^{3+} occupying oxygen dodecahedra and Fe^{3+} residing in octahedra/tetrahedra sites. Figure 2(c) presents a comparative estimate of the oxygen-vacancy formation probability as a function of cumulative electron dose [43], based on VASP-calculated formation energies E_c (3.53 eV for CFO, 3.81 eV for YIG) [44]. We emphasize that this calculation only provides a trend-level comparison rather than an absolute quantitative prediction. It can be seen that the red curve for CFO tends to require lower electron dose to achieves certain oxygen-vacancy formation probability than the blue curve for YIG. This trend agrees with the comparison of their experimental on-axis EELS spectra at Fe-$L_{2,3}$ edges changing with irradiation in Figs. 2(d) and 2(e). Under similar TEM conditions, YIG (3.78×10^9 e·nm^{-2}) shows negligible spectral change, while CFO (2.98×10^9 e·nm^{-2}) exhibits clear peak shifts and intensity variations, confirming that Fe^{3+} is less stabilized in CFO. In the following, systematic irradiation experiments will be performed on the beam-sensitive CFO.

2.2 Electron irradiation strategy

This part proposed an irradiation strategy for CFO, identifying critical electron dose and dose rate to balance SNR and beam damage. Figure 3 compares a series of on-axis EELS spectra under varying dose conditions. The corresponding raw data are provided in Fig. S1 in the Electronic Supplementary Material (ESM). On-axis EELS is used for excluding any influence from magnetism on spectral shape. The SNR is defined as the ratio of the L_3 peak intensity within the energy range [706 eV, 710 eV] after background subtraction to the standard deviation of the noise in the pre-edge region.

First, Figs. 3(a)–3(c) compare Fe-$L_{2,3}$ edges detected with a probe size of 2 nm and beam currents of 80, 40, and 20 pA corresponding to a dose rate of 3.98×10^7, 1.99×10^7, and 9.95×10^6 e·nm^{-2}·s^{-1}, respectively. The acquisition time is 40 s, making a single-acquisition dose of 1.59×10^9, 7.96×10^8, and 3.98×10^8 e·nm^{-2}, respectively. In each figure, two spectra were successively acquired at the same sample location with identical exposure times. At 80 pA in Fig. 3(a), significant changes were observed, including a 0.36 eV chemical shift toward lower energy losses and a 7.7% reduction in L_3 intensity, implying oxygen vacancy formation and the reduction of valence state of Fe ions [45, 46]. In Fig. 3(b) at 40 pA, L_3 intensity decreases by 4.5% with a less pronounced chemical shift. In contrast, Fig. 3(c) at 20 pA shows little change in the edge shape, though the SNR has decreased mainly from 129.26 in the 80 pA-40 s to 60.08 in the 20 pA-40 s.

Second, keeping the total dose reveals the impact of dose rates on the spectral shape and SNR. In Fig. 3(d), at 80 pA-10 s (same total dose as 20 pA-40 s), the L_3 intensity decreases by 4.4%, nearly matching the change in the case of 40 pA-40 s, suggesting that higher dose rates accelerate damage. This implies that the dose rate, rather than total dose alone, dominated CFO damage. The spectral evolution under 60 pA-20 s shown in Fig. S2 in the ESM further corroborates these findings. It agrees with the damage by the induced electric field (DIEF) mechanism, where exceeding threshold current densities trigger atomic displacement [42, 47, 48].

In addition, the beam current condition of 20 pA corresponding to a relatively low dose rate of 9.95×10^6 e·nm^{-2}·s^{-1} is maintained, and the exposure time is extended from 40 to 60 s. The spectral shape is still preserved in Fig. 3(e), and the SNR improves from 64.08 to 76.74. Extending to 80 s further improves SNR to 82.27, while a slight reduction in L_3 intensity (1.8%) can be seen in Fig. 3(f). Even so, this beam damage is weaker compared to the 40 pA-40 s case. In the following, the condition of 20 pA-60 s is used for EMCD experiments.

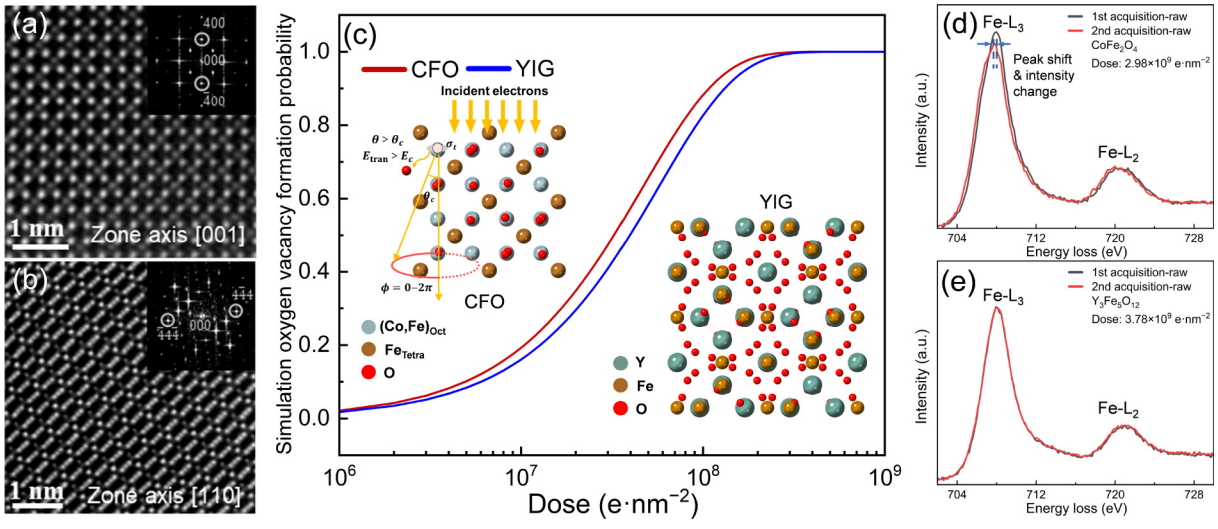

Figure 2 Comparison of the beam-sensitivity of CFO and YIG structures. (a) and (b) Atomic-resolution HAADF-STEM images. (c) VASP-calculated correlation between electron dose and oxygen vacancy formation probability. (d) and (e) Conventional on-axis EELS spectra were consecutively acquired twice.

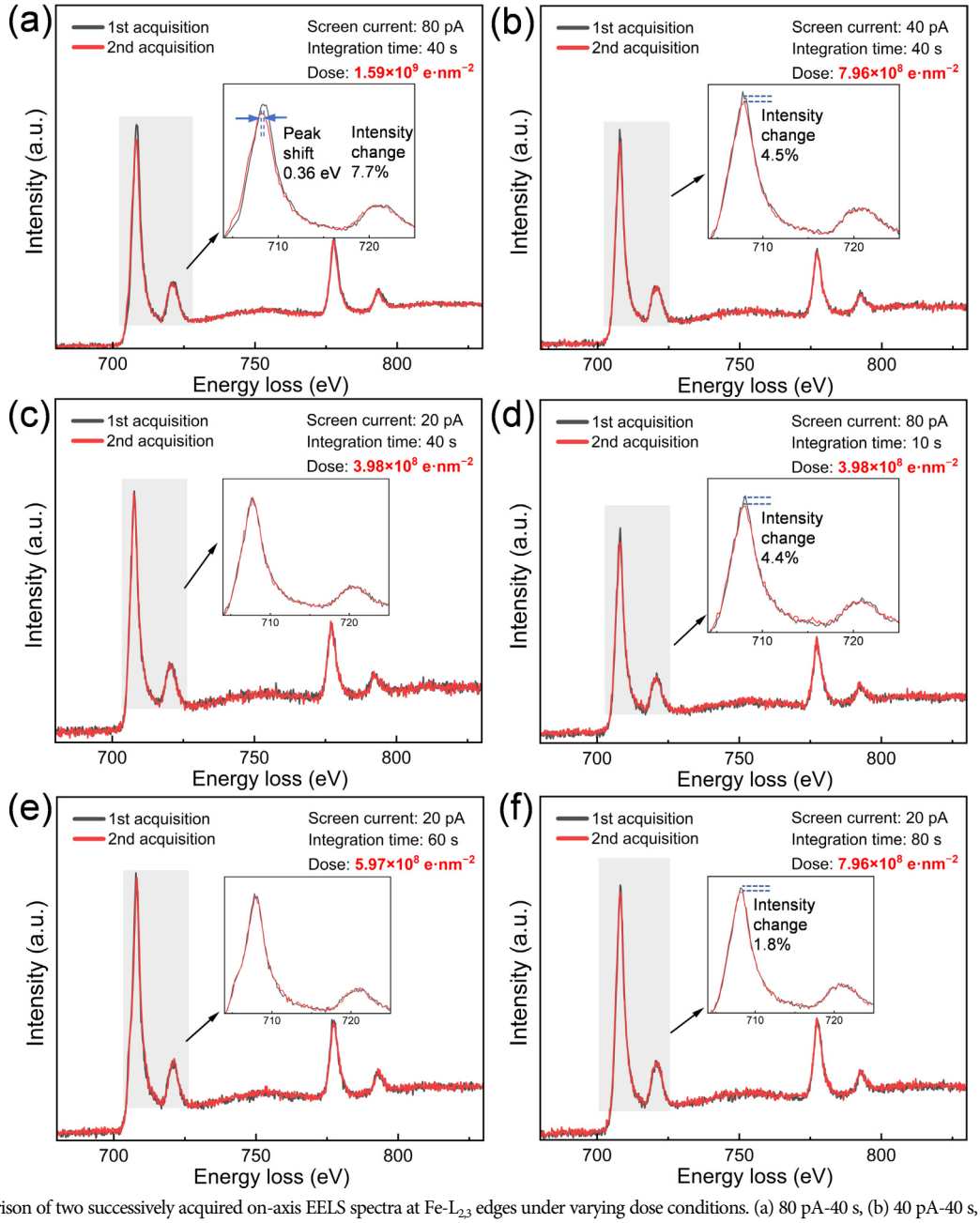

Figure 3 Comparison of two successively acquired on-axis EELS spectra at Fe-$L_{2,3}$ edges under varying dose conditions. (a) 80 pA-40 s, (b) 40 pA-40 s, (c) 20 pA-40 s, (d) 80 pA-10 s, (e) 20 pA-60 s, and (f) 20 pA-80 s.

These findings suggest that reducing the dose rate and extending the exposure time effectively suppresses defect formation and improves the SNR. This provides a practical dose-control strategy for EELS and EMCD studies in beam-sensitive oxides.

2.3 Correction methods of EMCD artifacts for beam-sensitive oxides

An optimized dose condition of 20 pA-60 s is set for CFO considering beam damage, yet **q**-EELS at 20 pA suffers from low SNR due to much smaller off-axis apertures, often obscuring EMCD signals. As mentioned above in the "method design and model structure" part, adjusting the aperture position towards diffraction spots can increase **q**-EELS signal intensity and SNR, while easily introduces artifacts into EMCD spectra.

The artifacts can be explained and quantified with simulations based on theories of Bloch wave and inelastic electron scattering [31, 39]. In theory, **q**-EELS intensity can be described by the double differential scattering cross-section (DDSCS) in Eq. (1) [49].

$$\frac{\partial^2\sigma}{\partial\Omega\partial E}=\sum_q\frac{A^{\mathrm{det}}_{q;q}}{q^4}\cdot S\left(\boldsymbol{q},\boldsymbol{q}'\right)+\sum_q\sum_{q'\neq q}2\times\mathrm{Re}\left[\frac{A^{\mathrm{det}}_{q;q}}{q^4}S\left(\boldsymbol{q},\boldsymbol{q}'\right)\right] \quad (1)$$

The term $A^{\mathrm{det}}_{q;q}/q^4$ represents the product of the corrected Bloch wave coefficients for the incident and scattered detected electrons, where $\boldsymbol{q}$ and $\boldsymbol{q}'$ denote the momentum transfer vectors. A mixed dynamic form factor (MDFF) $S\left(\boldsymbol{q},\boldsymbol{q}'\right)$ appearing in Eq. (1) and simply expressed in Eq. (2) has a real component $a\left(\boldsymbol{q}\cdot\boldsymbol{q}'\right)$, representing non-magnetic contributions, and an imaginary

component $ib(\boldsymbol{q}\times\boldsymbol{q}')$, containing magnetic information. The vector $\boldsymbol{e_B}$ in it is the unit vector of the external magnetic field, typically generated by the objective lens.

$$S(\boldsymbol{q},\boldsymbol{q}') = \frac{a(\boldsymbol{q}\cdot\boldsymbol{q}') + ib(\boldsymbol{q}\times\boldsymbol{q}')\cdot\boldsymbol{e_B}}{\boldsymbol{q}^2\boldsymbol{q}'^2} \quad (2)$$

The equations indicate that the **q**-EELS at any diffraction-plane point includes both nonmagnetic and magnetic signals, and the **q**-EELS intensity distributions can be strongly modulated by dynamic electron diffraction conditions. For the CFO specimen (~ 30 nm thick), tilted by 7° from the [001] zone axis to establish a ±(400) three-beam condition, reciprocal-space DDSCS maps were simulated. Then, the reciprocal space map of the magnetic EMCD signal at the Fe-L_3 edge, as shown in Fig. 4(a), can be obtained by subtracting the imaginary DDSCS components of the lower half from those of the upper half, using the ±(400) diffraction row as a symmetry axis. The map of the nonmagnetic signal as shown in Fig. 4(b) is extracted in a same way from the real components of DDSCS.

Both maps exhibit spatial asymmetry. The asymmetry in Fig. 4(a) reflects the ideal EMCD signal, whereas the nonmagnetic asymmetry in Fig. 4(b) represents an experimental artifact. In addition, the magnetic EMCD signal decays rapidly near diffraction spots, while non-magnetic signals exhibit maximum intensity in these regions. As a result, placing the aperture near the spots (solid circle) leads to overestimation of the EMCD signal at the Fe-L_3 edge, while the L_2 edge is underestimated due to the reverse EMCD sign compared with L_3 case and the unchanged nonmagnetic asymmetry. In other words, the detected Fe-$L_{2,3}$ intensity of pos+ is like artificially elevated and pos- suppressed, producing artifacts in the final EMCD spectrum.

As compared in Fig. 4(c), although conventional aperture placement like the dashed circles in Figs. 4(a) and 4(b) largely avoids these artifacts, it yields poor SNR of 15.58 under limited electron dose, while positioning a larger aperture closer to diffraction spots like the solid circles improves SNR to 23.08 but introduces nonmagnetic asymmetry that must be corrected. This asymmetry may be mitigated experimentally via a double-difference procedure [50, 51], while this procedure requires double dose, making it not applicable to the beam-sensitive cases.

In this work, the EMCD signal was intentionally acquired in the solid-aperture region as shown in Figs. 4(a) and 4(b) to improve the SNR in low dose cases. Actually, the commonly used post-edge normalization procedure can partly remove the asymmetry-induced artifacts. The reason why the post-edge normalization cannot make a full removal is that the sensitivity of the $L_{2,3}$ edges to changes in dynamic diffraction conditions can hardly be the same with the sensitivity of the post edge. Then, the correction of the residual asymmetry-induced artifacts is anchored experimentally using the non-magnetic O-K edge.

Figure 4(d) shows two post-edge-normalized **q**-EELS spectra at the O-K edge acquired at EMCD positions (pos+ and pos−), where a small but systematic intensity difference is clearly resolved. There can be a correction factor $k = I^{pos-}_{O\text{-}K}/I^{pos+}_{O\text{-}K}$, defined as the ratio of two integrated O-K edge intensities at two EMCD positions. For instance, the k in Fig. 4(d) is 0.985. This experimentally determined factor can then be applied to further normalize the post-edge-normalized Fe-$L_{2,3}$ **q**-EELS spectra. Although the Fe 3d and O 1s states behave differently in anisotropy, such correction can still contribute to reduce the asymmetry-induced artifacts. Note that a same correction factor k is applied to L_3 and L_2 edges, as in this work we consider L_3 and L_2 edges are similarly sensitive to dynamic electron diffraction changes.

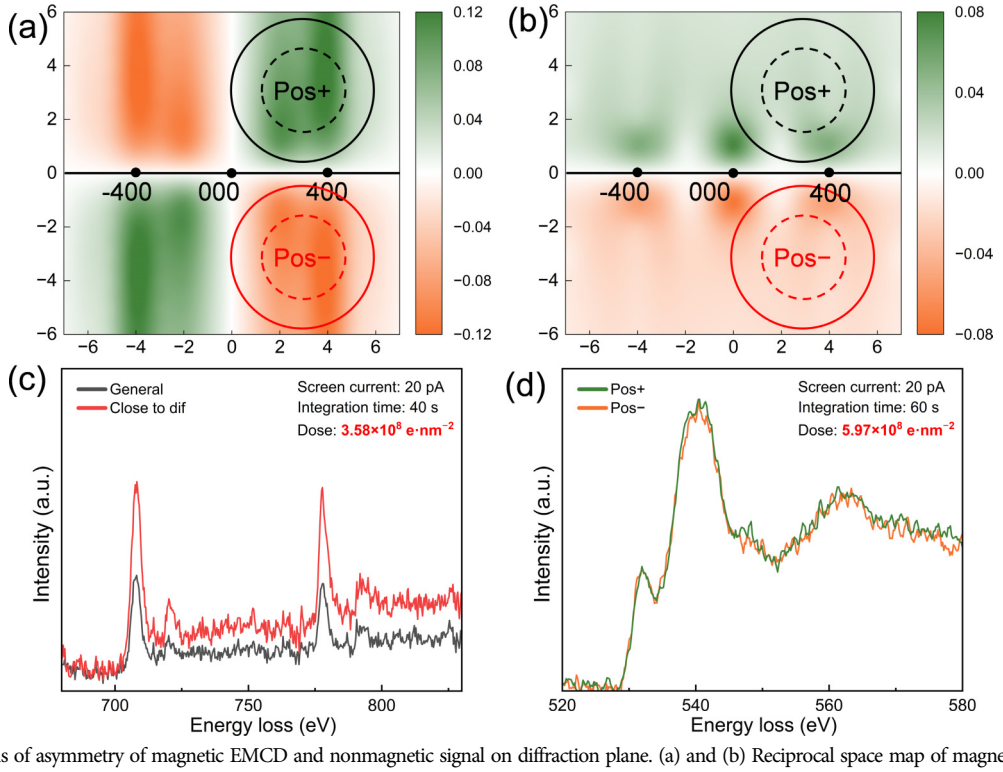

Figure 4 Simulations of asymmetry of magnetic EMCD and nonmagnetic signal on diffraction plane. (a) and (b) Reciprocal space map of magnetic and nonmagnetic signal at the Fe-L_3 edge, respectively, for the CFO structure in a ±(400) three-beam condition and with the thickness of ~ 30 nm. (c) Comparison of experimental EELS spectra acquired with apertures like solid circles and dashed circles. (d) Comparison of the O-K edges extracted from the normalized **q**-EELS spectra acquired at pos+ and pos− under identical experimental conditions (20 pA-60 s).

2.4 Post-processing method improving quantification precision

Despite of the optimization proposed above, the noise level of EMCD is still higher than conventional on-axis EELS spectra, therefore inherently limiting the precision of magnetic moment quantification from EMCD spectra. To address this, a joint-parameter processing (JPP) method is proposed.

Figure 5(a) presents a simplified noise-free EELS model of Fe-$L_{2,3}$ edges composed of mathematical functions, providing greater details than our Fe-$L_{2,3}$ models previously reported in our previous work in Ref. [47]. The background curve in blue is described by an inverse power law, $f_B = Ax^{-r}$ (r = 3.6, fixed for noise-free spectra in Fig. 5) and peaks by several Gaussian functions. The inset of Fig. 5(b) presents two **q**-EELS spectra generated from this model, with Gaussian noises of identical level added. Their backgrounds are $f_{B\text{pos}+} = A_1x^{-r} + \delta_1$ and $f_{B\text{pos}-} = A_2x^{-r} + \delta_2$, where δ_1 and δ_2 are noises and the possible difference in A_1 and A_2 reflects the asymmetrical background intensity. The true m_l/m_s value of 0.09 is set as an example.

The EMCD post-processing commonly applies independent parameter processing (IPP) approach, where the same pre-edge window is used to fit the backgrounds of two noisy **q**-EELS spectra separately. Noise causes deviations in the fitted r values, so discrepancies arise in the background subtraction between two **q**-EELS spectra. This introduces significant errors in the EMCD signal intensity and moment quantification. As shown in Fig. 5(b), at a noise level of 10 which is comparable to that of the experimental spectra in Fig. 6, the m_l/m_s ratio of 0.28 calculated via IPP method can substantially deviate from the set actual value of 0.09. This effect is clearly reflected in the green error bars in Fig. 5(d). Each error bar was derived from 100 simulated pairs of **q**-EELS spectra at the same noise level, with 15 error bars covering noise levels ranging from 0.002 to 0.027. The noise level is defined as the ratio of the Fe-L_3 peak maximum to the standard deviation of the pre-edge noise after background subtraction.

The proposed JPP method reduces these errors by jointly fitting the background of two **q**-EELS. First, two **q**-spectra are summed to form a new one, as in Eq. 3. Taking logarithms on both sides, the r becomes a coefficient of a linear equation in Eq. 4. This log-transformed approach offers improved numerical stability and reduced sensitivity to noise compared to direct exponential fitting. The δ is negligible compared with the signal after natural logarithm operation.

$$f_B = f_{B\text{pos}+} + f_{B\text{pos}-} = (A_1 + A_2) \times x^{-r} + \delta_1 + \delta_2 = (A_1 + A_2) \times x^{-r} + \delta \quad (3)$$

$$\ln f_B = \ln[(A_1 + A_2) \times x^{-r} + \delta] \approx \ln[(A_1 + A_2) \times x^{-r}] = \ln(A_1 + A_2) - r \times \ln x \quad (4)$$

This allows determination of a single fitted parameter r_{fit} by fitting the linear equation. Next, r_{fit} value is applied to $f_{B\text{pos}+} = A_1 \times x^{-r_{\text{fit}}}$ and $f_{B\text{pos}-} = A_2 \times x^{-r_{\text{fit}}}$ to fit the A_1 and A_2. Now two fitted functions are determined. Figure 6(c) is obtained by background removal using the two determined functions,

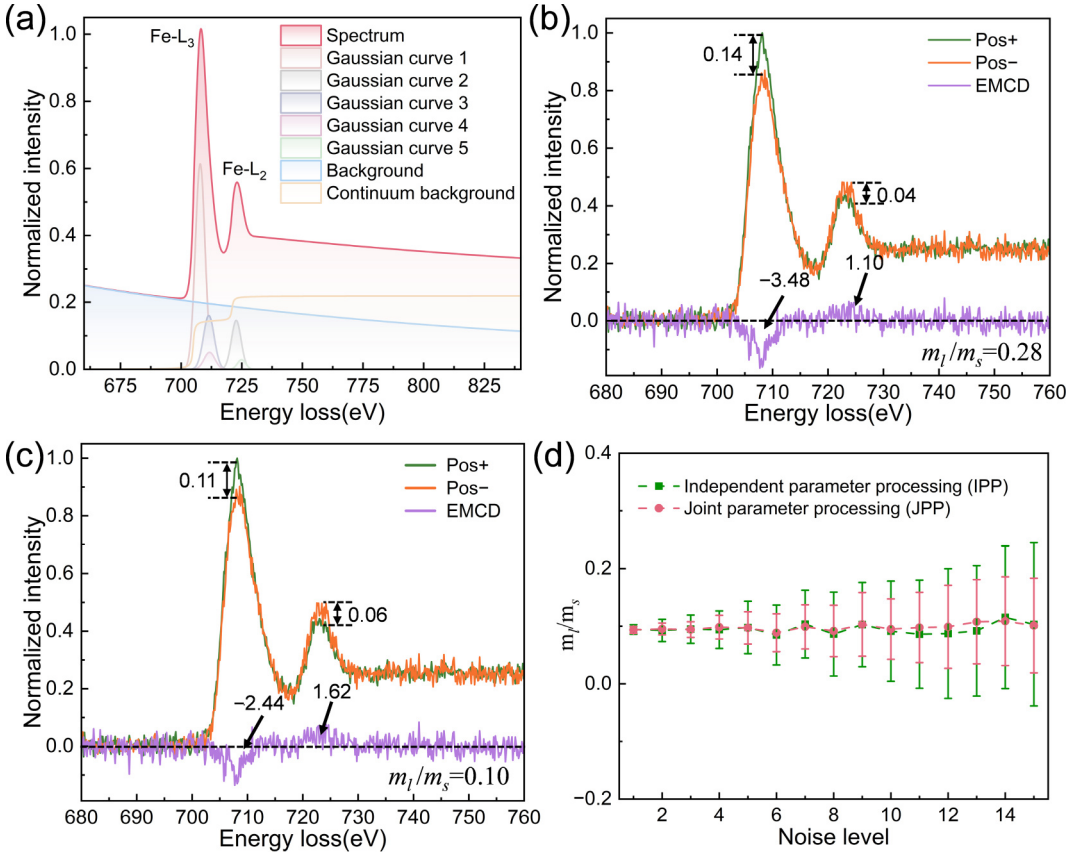

Figure 5 A simulation study of noise-dependent EMCD quantification precision with different post-processing methods. (a) A mathematical model of Fe-$L_{2,3}$ edges. (b) **q**-EELS spectra and EMCD signals obtained with the IPP process at a noise level of 10; the inset shows **q**-EELS spectra before background removal. (c) Spectra obtained with the JPP process at a noise level of 10. (d) Statistics of m_l/m_s values obtained from 100 data for each noise level treated with IPP and JPP processes.

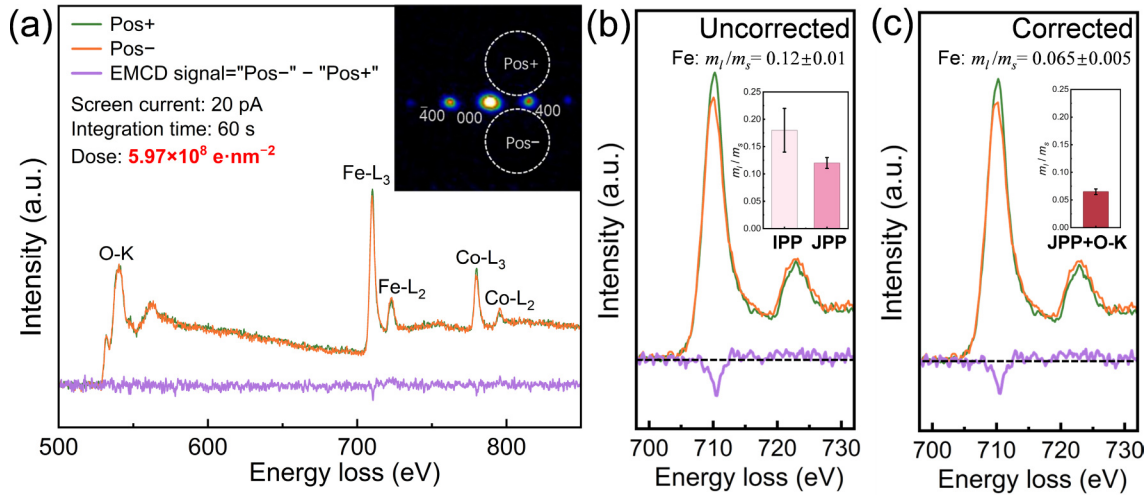

Figure 6 Experimental EMCD signal (filtered) of Fe and Co before and after correction. (a) Two **q**-EELS and EMCD spectra containing O-K, Fe-L, and Co-L edges. (b) Enlarged EMCD signal of Fe applying the JPP method. (c) EMCD signal corrected applying both JPP method and O-K edge normalization. Statistical values can be seen in Table S1 in the ESM.

performed on the same **q**-EELS pair in the inset of Fig. 6(b). In contrast, two methods yield different values of m_l/m_s (0.28 and 0.10) as well as different peak intensities (0.14 and 0.11) and integrated edge intensities (−3.48 and −2.44). The difference can be more clearly seen in Fig. 6(d), in which red error bars are obtained with the JPP method. For examples, IPP yields m_l/m_s values of 0.094 ± 0.008, 0.098 ± 0.046, 0.091 ± 0.087, 0.103 ± 0.142 for the noise levels of 1, 5, 10 and 15, whereas JPP gives 0.094 ± 0.005, 0.097 ± 0.028, 0.095 ± 0.052, 0.101 ± 0.082, corresponding to a decrease of error bars by approximately 40% while a similar mean value. It indicates that the JPP method remarkably enhances quantitative precision without compromising accuracy.

2.5 EMCD experimental

Figure 6 presents the experimental EMCD results using the optimized dose condition and proposed aperture positions. Note that these spectra are filtered for presentation, while the quantification results are obtained with raw data. Actually, according to Ref. [52], the quantification value will not change even with filtering. In Fig. 6(a), two **q**-EELS spectra show simultaneous presence of the O-K, Fe-$L_{2,3}$, and Co-$L_{2,3}$ edges. No chemical shifting is observed for any of the three elements, and O-K edges are superimposed, verifying that the observed differences between the two **q**-EELS spectra at Fe-L and Co-L peaks are not due to a valence state change during the irradiation. The purple EMCD spectrum, which is the difference of the two **q**-EELS after background subtraction using JPP method proposed in Section 2.4, exhibits negative peaks at Fe-L_3 and Co-L_3 while positive peaks at Fe-L_2 and Co-L_2, indicating non-zero magnetic moments for both Fe and Co atoms. Then, the pre-edge background of Fe-$L_{2,3}$ edges is also removed using the JPP method, and an EMCD signal of Fe is obtained in Fig. 6(b). The quantified result is m_l/m_s = 0.12 ± 0.01, in which the error ± 0.01 is estimated by varying the window width for pre-edge background subtraction. Statistical values can be seen in Table S1 in the ESM. Note that it is in sharp contrast with m_l/m_s = 0.18 ± 0.04 obtained with the common IPP method, indicating the effectiveness of JPP method in experimental spectra.

Figures 6(b) and 6(c) compare EMCD signals of Fe before and after correction referring to O-K edges. Figure 6(b) exhibits relatively strong Fe-L_3 and weak Fe-L_2 intensity in the EMCD spectrum. The reason has been detailly explained in Fig. 4. After corrections with k = 0.985, Fig. 6(c) displays reduced Fe-L_3 intensity and enhanced Fe-L_2 visibility, yielding a revised value of m_l/m_s = 0.065 ± 0.005 that aligns more closely with reported X-ray magnetic circular dichroism (XMCD) literature values [53, 54]. This implies the critical necessity of artifact correction for quantitative EMCD analysis in beam-sensitive materials.

3 Conclusions

In conclusion, the methodological advances developed in this work—including the dose strategy tailoring dose rate, aperture-based SNR enhancement combined with an artifact correction method, and JPP-based post-processing method—establish a comprehensive framework for quantitative EMCD studies of beam-sensitive oxides. Within the framework, simultaneous and reliable EMCD measurements of Fe and Co in beam-sensitive $CoFe_2O_4$ has been obtained. Importantly, a significant improvement in the m_l/m_s quantitative precision has been achieved with our developed JPP post-processing method, tackling the challenge of high-noise EMCD spectra in limited dose conditions. In addition, the correction based on O-K edge normalization effectively suppresses residual asymmetry-induced artifacts without applying model-dependent corrections. This framework substantially extends the applicability of EMCD to spin-orbit coupling studies in a broader range of magnetic oxides and provides new opportunities for advancing spintronic material design.

4 Experimental section

4.1 Sample preparation

A $CoFe_2O_4$ (CFO) thin film, used as a model sample in this work, was epitaxially grown on a $SrTiO_3$ (001) substrate by molecular-beam epitaxy. A commercial $Y_3Fe_5O_{12}$ (YIG) thin film was used as a reference sample. Cross-sectional TEM specimens were prepared using a Thermo Scientific Helios 5 CX focused ion beam (FIB) system equipped with a Ga^+ ion source. Final thinning was carried out by successive low-energy ion polishing at 2 kV/10 pA and 1 kV/16 pA to minimize surface amorphization. Prior to TEM observation, the specimens were plasma-cleaned sequentially with

Ar/O_2 and SF_6 plasmas to remove organic residues, silicon oxides, and hydrocarbon contaminants.

4.2 TEM experiments

TEM experiments were performed on a Thermo Fisher Spectra 300 STEM operated at 300 kV, equipped with a high-brightness Schottky field-emission gun with monochromator (X-FEG UltiMono), probe and image Cs correctors, an energy filter (Gatan 1066 GIF), and a K3 direct electron detection camera. EELS spectra were acquired with a C2 aperture of 20 μm, a semi-convergence angle of 500 μrad, a camera length of 115 mm, and a probe size of 9. The width of half maximum of the probe is about 2 nm (see Fig. S3 in the ESM). EMCD measurements were performed under the ±(400) three-beam condition on a region approximately 30 nm in thickness, as determined from on-axis low-loss EELS spectra.

4.3 Simulations

The development of the artifact removal method is based on simulations of elastic and inelastic electron scattering. Variations in EMCD signal intensity with sample thickness and crystal orientation can be modeled with the "bw" code [55], developed within the Bloch Wave framework. In addition, in-house C++ and MATLAB codes were designed to simulate reciprocal space maps of the EMCD signal and identify the asymmetric nonmagnetic components responsible for artifacts. All simulations were made in ±(400) three-beam conditions of the CFO structure. These simulations were then used to correct experimental EMCD spectra. As high-noise-level EMCD spectra are common in the condition of limited electron dose, an in-house MATLAB codes were developed to establish a post-processing method that can improve the quantification precision for high-noise-level EMCD spectra.

In addition, as a reference for irradiation strategy, the correlation between electron dose and oxygen vacancy formation probability was estimated with density functional theory (DFT). DFT calculations were carried out using Vienna *ab initio* simulation package (VASP). The exchange-correlation energy of the CFO and YIG systems was described using the Perdew–Burke–Ernzerhof (PBE) functional within the framework of the generalized gradient approximation (GGA). Detailed parameters in simulations and calculations can be seen in the ESM.

Electronic Supplementary Material: Supplementary material (the raw data of conventional core-level EELS spectra under different conditions before and after irradiation, the probe size, the statistical values of m_l/m_s, and the detailed parameters and methodologies for DFT calculations) is available in the online version of this article at https://doi.org/10.26599/NR.2026.94908566.

Data availability

The data that support the findings of this study are available within the article and its Electronic Supplementary Material. Other relevant data that support the findings of this study are available from the corresponding author upon reasonable request.

Acknowledgements

This work is supported by the National Key Research and Development Program of China (Nos. 2021YFB3702101 and 2024YFA1208002), the Natural Science Foundation of Chongqing (No. CSTB2025NSCQ-GPX0763), and the National Natural Science Foundation of China (No. 12374108).

Declaration of competing interest

All the contributing authors report no conflicts of interest in this work.

Author contribution statement

Z. X. Z.: Investigation, writing – original draft. X. X. F.: Data curation, funding acquisition, investigation, methodology, project administration, supervision, writing – review & editing. J. J. L.: Investigation & software. H. C. D.: Investigation. Y. Z.: Software. P. T.: Software. F. Y. C.: Methodology. L. F. S.: Methodology. R. W.: Resources. D. L. Z.: Reviewing & visualization. X. X. H.: Visualization, reviewing and editing, funding acquisition. All authors have given approval to the final version of the manuscript.

Use of AI statement

None.

References

[1] Coronado, E. Molecular magnetism: From chemical design to spin control in molecules, materials and devices. *Nat. Rev. Mater.* **2020**, *5*, 87–104.

[2] Fischer, M. H.; Sigrist, M.; Agterberg, D. F.; Yanase, Y. Superconductivity and local inversion-symmetry breaking. *Annu. Rev. Condens. Matter. Phys.* **2023**, *14*, 153–172.

[3] Kumar, D.; Jin, T. L.; Sbiaa, R.; Kläui, M.; Bedanta, S.; Fukami, S.; Ravelosona, D.; Yang, S. H.; Liu, X. X.; Piramanayagam, S. N. Domain wall memory: Physics, materials, and devices. *Phys. Rep.* **2022**, *958*, 1–35.

[4] Chen, H. T.; Yi, D. Spin-charge conversion in transition metal oxides. *APL Mater.* **2021**, *9*, 060908.

[5] Zheng, D. X.; Fang, Y. W.; Wen, Y.; Song, K. P.; Li, Y.; Fang, B.; Zhang, C. H.; Chen, A. T.; Liu, C.; Algaidi, H. et al. Field-free switching of magnetization in oxide superlattice by engineering the interfacial reconstruction. *Adv. Funct. Mater.* **2024**, *34*, 2312746.

[6] Zhou, G. W.; Ji, H. H.; Kang, P. H.; Dou, J. R.; Wang, S. Q.; Xu, X. H. Overview of magnetic anisotropy evolution in $La_{2/3}Sr_{1/3}MnO_3$-based heterostructures. *Sci. China Mater.* **2023**, *66*, 3401–3414.

[7] Nordlander, J.; Anderson, M. A.; Brooks, C. M.; Holtz, M. E.; Mundy, J. A. Epitaxy of hexagonal ABO_3 quantum materials. *Appl. Phys. Rev.* **2022**, *9*, 031309.

[8] Yi, D.; Liu, J.; Hsu, S. L.; Zhang, L. P.; Choi, Y.; Kim, J. W.; Chen, Z. H.; Clarkson, J. D.; Serrao, C. R.; Arenholz, E. et al. Atomic-scale control of magnetic anisotropy via novel spin-orbit coupling effect in $La_{2/3}Sr_{1/3}MnO_3/SrIrO_3$ superlattices. *Proc. Natl. Acad. Sci. USA* **2016**, *113*, 6397–6402.

[9] Mellinger, C.; Waybright, J.; Zhang, X. Z.; Schmidt, C.; Xu, X. S. Perpendicular magnetic anisotropy in conducting $NiCo_2O_4$ films from spin-lattice coupling. *Phys. Rev. B* **2020**, *101*, 014413.

[10] Guo, J. R.; He, B.; Han, Y.; Liu, H.; Han, J. L.; Ma, X. Q.; Wang, J. Q.; Gao, W. Q.; Lü, W. M. Resurrected and tunable conductivity and ferromagnetism in the secondary growth $La_{0.7}Ca_{0.3}MnO_3$ on transferred $SrTiO_3$ membranes. *Nano Lett.* **2024**, *24*, 1114–1121.

[11] Wang, Z. Y.; Zhu, Z. H.; Yang, H.; Sun, F.; Zhang, Y.; Zhang, X. Y.; Zhang, B. M.; Zheng, Y. Edge dislocation with [001] $\vec{b}$ induced positive magnetoresistance in $BaTiO_3/La_{0.66}Sr_{0.33}MnO_3$ heterostructure. *Acta Mater.* **2024**, *275*, 120054.

[12] Granada, M.; Sánchez, J. C. R.; Steren, L. B. Giant magnetoresistance

in oxide-based metallic multilayers. *Appl. Phys. Lett.* **2007**, *91*, 072110.

[13] Schattschneider, P.; Rubino, S.; Hébert, C.; Rusz, J.; Kuneš, J.; Novák, P.; Carlino, E.; Fabrizioli, M.; Panaccione, G.; Rossi, G. Detection of magnetic circular dichroism using a transmission electron microscope. *Nature* **2006**, *441*, 486–488.

[14] Song, D. S.; Wang, Z. Q.; Zhu, J. Magnetic measurement by electron magnetic circular dichroism in the transmission electron microscope. *Ultramicroscopy* **2019**, *201*, 1–17.

[15] Ali, H.; Rusz, J.; Bürgler, D. E.; Vas, J. V.; Jin, L.; Adam, R.; Schneider, C. M.; Dunin-Borkowski, R. E. Visualizing subatomic orbital and spin moments using a scanning transmission electron microscope. *Nat. Mater.* **2025**, *24*, 1215–1220.

[16] Thersleff, T.; Muto, S.; Werwiński, M.; Spiegelberg, J.; Kvashnin, Y.; Hjörvarsson, B.; Eriksson, O.; Rusz, J.; Leifer, K. Towards sub-nanometer real-space observation of spin and orbital magnetism at the Fe/MgO interface. *Sci. Rep.* **2017**, *7*, 44802.

[17] Zeng, Z.; Fu, X.; Hu, Q.; Liu, G.; Li, J.; Huang, X. The influence of residual plural scattering after deconvolution in electron magnetic chiral dichroism. *Ultramicroscopy* **2023**, *253*, 113806.

[18] Hu, Q.; Fu, X.; Zeng, Z.; Li, J.; Liu, G.; Zheng, C.; Zhang, L.; Huang, X. Electron knock-on damage effects on electron magnetic chiral dichroism of magnetic metals using cobalt as a model. *Appl. Phys. Lett.* **2024**, *124*, 092407.

[19] Song, D. S.; Tavabi, A. H.; Li, Z. A.; Kovács, A.; Rusz, J.; Huang, W. T.; Richter, G.; Dunin-Borkowski, R. E.; Zhu, J. An in-plane magnetic chiral dichroism approach for measurement of intrinsic magnetic signals using transmitted electrons. *Nat. Commun.* **2017**, *8*, 15348.

[20] Fu, X.; Warot-Fonrose, B.; Arras, R.; Dumesnil, K.; Serin, V. Quantitative moment study and coupling of 4f rare earth and 3d metal by transmitted electrons. *Phys. Rev. B* **2016**, *94*, 140416.

[21] Ennen, I.; Löffler, S.; Kübel, C.; Wang, D.; Auge, A.; Hütten, A.; Schattschneider, P. Site-specific chirality in magnetic transitions. *J. Magn. Magn. Mater.* **2012**, *324*, 2723–2726.

[22] Warot-Fonrose, B.; Gatel, C.; Calmels, L.; Serin, V.; Snoeck, E.; Cherifi, S. Magnetic properties of FeCo alloys measured by energy-loss magnetic chiral dichroism. *J. Appl. Phys.* **2010**, *107*, 09D301.

[23] Makino, H.; Rusz, J.; Wang, J.; Turenne, D.; Ohtsuka, M.; Takahashi, Y. K.; Dürr, H. A.; Muto, S. A study on the relationship of magnetic moments orientation in $L1_0$ FePt network nanostructured film by electron energy-loss magnetic chiral dichroism using semi-core excitation spectra. *J. Magn. Magn. Mater.* **2022**, *558*, 169522.

[24] Fu, X.; Warot-Fonrose, B.; Arras, R.; Demaille, D.; Eddrief, M.; Etgens, V.; Serin, V. Energy-loss magnetic chiral dichroism study of epitaxial MnAs film on GaAs(001). *Appl. Phys. Lett.* **2015**, *107*, 062402.

[25] Fu, X.; Warot-Fonrose, B.; Arras, R.; Seine, G.; Demaille, D.; Eddrief, M.; Etgens, V.; Serin, V. *In situ* observation of ferromagnetic order breaking in MnAs/GaAs(001) and magnetocrystalline anisotropy of α-MnAs by electron magnetic chiral dichroism. *Phys. Rev. B* **2016**, *93*, 104410.

[26] He, M.; He, X.; Lin, L.; Song, B.; Zhang, Z. H. Study on spin polarization of non-magnetic atom in diluted magnetic semiconductor: The case of Al-doped 4H–SiC. *Solid State Commun.* **2014**, *197*, 44–48.

[27] Zhang, Z. H.; Tao, H. L.; He, M.; Li, Q. Origination of electron magnetic chiral dichroism in cobalt-doped ZnO dilute magnetic semiconductors. *Scripta Mater.* **2011**, *65*, 367–370.

[28] del-Pozo-Bueno, D.; Varela, M.; Estrader, M.; López-Ortega, A.; Roca, A. G.; Nogués, J.; Peiró, F.; Estradé, S. Direct evidence of a graded magnetic interface in bimagnetic core/shell nanoparticles using electron magnetic circular dichroism (EMCD). *Nano Lett.* **2021**, *21*, 6923–6930.

[29] Loukya, B.; Negi, D. S.; Dileep, K.; Pachauri, N.; Gupta, A.; Datta, R. Effect of Bloch wave electron propagation and momentum-resolved signal detection on the quantitative and site-specific electron magnetic chiral dichroism of magnetic spinel oxide thin films. *Phys. Rev. B* **2015**, *91*, 134412.

[30] Wang, Z. Q.; Zhong, X. Y.; Yu, R.; Cheng, Z. Y.; Zhu, J. Quantitative experimental determination of site-specific magnetic structures by transmitted electrons. *Nat. Commun.* **2013**, *4*, 1395.

[31] Song, D. S.; Wang, Z. Q.; Zhu, J. Effect of the asymmetry of dynamical electron diffraction on intensity of acquired EMCD signals. *Ultramicroscopy* **2015**, *148*, 42–51.

[32] Wang, Z. C.; Tavabi, A. H.; Jin, L.; Rusz, J.; Tyutyunnikov, D.; Jiang, H. B.; Moritomo, Y.; Mayer, J.; Dunin-Borkowski, R. E.; Yu, R. et al. Atomic scale imaging of magnetic circular dichroism by achromatic electron microscopy. *Nat. Mater.* **2018**, *17*, 221–225.

[33] Yao, L. D.; Majumdar, S.; Äkäslompolo, L.; Inkinen, S.; Qin, Q. H.; van Dijken, S. Electron-beam-induced perovskite-brownmillerite-perovskite structural phase transitions in epitaxial $La_{2/3}Sr_{1/3}MnO_3$ films. *Adv. Mater.* **2014**, *26*, 2789–2793.

[34] Jang, J. H.; Kim, Y. M.; He, Q.; Mishra, R.; Qiao, L.; Biegalski, M. D.; Lupini, A. R.; Pantelides, S. T.; Pennycook, S. J.; Kalinin, S. V. et al. *In situ* observation of oxygen vacancy dynamics and ordering in the epitaxial $LaCoO_3$ system. *ACS Nano* **2017**, *11*, 6942–6949.

[35] Dong, Z. H.; Qian, L. B.; Li, Q. F.; Liu, Z.; Guo, J. C.; Wang, L.; Wu, S. H.; Xiong, R.; Liu, Y.; He, C. Q. Coexistence of volatile and non-volatile resistive switching characteristics in NbO_x memristor regulated by electron irradiation-induced surface oxygen vacancies. *Appl. Surf. Sci.* **2025**, *687*, 162295.

[36] Kumar, M.; Ahn, Y. H.; Iqbal, S.; Kim, U.; Seo, H. Site-specific regulated memristors via electron-beam-induced functionalization of HfO_2. *Small* **2022**, *18*, 2105585.

[37] Ran, K.; Zeng, F. L.; Jin, L.; Baumann, S.; Meulenberg, W. A.; Mayer, J. *In situ* observation of reversible phase transitions in Gd-doped ceria driven by electron beam irradiation. *Nat. Commun.* **2024**, *15*, 8156.

[38] Zhang, Y.; Wang, Y. P.; Wu, Y. S.; Shu, X. Y.; Zhang, F.; Peng, H. N.; Shen, S. C.; Ogawa, N.; Zhu, J. Y.; Yu, P. Artificially controlled nanoscale chemical reduction in VO_2 through electron beam illumination. *Nat. Commun.* **2023**, *14*, 4012.

[39] Rusz, J. Role of symmetry in quantitative EMCD experiments. *arXiv preprint arXiv:* **0910**, *3849*, 2009.

[40] Fang, Y.; Mullurkara, S.; Taddei, K. M.; Ohodnicki, P. R.; Wang, G. F. Machine learning enabled accurate prediction of structural and magnetic properties of cobalt ferrite. *npj Comput. Mater.* **2025**, *11*, 103.

[41] Zhang, Y.; Zhang, Y. Y.; Li, C. E.; Yan, X. H.; Hu, S.; Yin, R. B.; Wei, Y. F.; Gao, K. Z.; Gao, H. L. Research progress of $NiFe_2O_4$ electrode materials in supercapacitors: Preparation, modification, structural regulation, and future challenges. *Coordin. Chem. Rev.* **2024**, *519*, 216103.

[42] Jiang, N. Electron beam damage in oxides: A review. *Rep. Prog. Phys.* **2016**, *79*, 016501.

[43] Xing, W. D.; Sha, H. Z.; Meng, F. Y.; Yu, R. Defect structures of the $Cr_2O_3(11\bar{2}0)$ surface: Effect of electron beam irradiation. *J. Mater. Chem. C* **2021**, *9*, 6324–6331.

[44] Egerton, R. F.; Li, P.; Malac, M. Radiation damage in the TEM and SEM. *Micron* **2004**, *35*, 399–409.

[45] Paterson, J. H.; Krivanek, O. L. Elnes of 3d transition-metal oxides: II Variations with oxidation state and crystal structure. *Ultramicroscopy* **1990**, *32*, 319–325.

[46] Tan, H. Y.; Verbeeck, J.; Abakumov, A.; Van Tendeloo, G. Oxidation state and chemical shift investigation in transition metal oxides by EELS. *Ultramicroscopy* **2012**, *116*, 24–33.

[47] Jiang, N.; Spence, J. C. H. On the dose-rate threshold of beam damage in TEM. *Ultramicroscopy* **2012**, *113*, 77–82.
[48] Jiang, N. Structure and composition dependence of oxygen K edge in $CaAl_2O_4$. *J. Appl. Phys.* **2006**, *100*, 013703.
[49] Calmels, L.; Houdellier, F.; Warot-Fonrose, B.; Gatel, C.; Hÿtch, M. J.; Serin, V.; Snoeck, E.; Schattschneider, P. Experimental application of sum rules for electron energy loss magnetic chiral dichroism. *Phys. Rev. B* **2007**, *76*, 060409.
[50] Lidbaum, H.; Rusz, J.; Liebig, A.; Hjörvarsson, B.; Oppeneer, P. M.; Coronel, E.; Eriksson, O.; Leifer, K. Quantitative magnetic information from reciprocal space maps in transmission electron microscopy. *Phys. Rev. Lett.* **2009**, *102*, 037201.
[51] Rusz, J.; Lidbaum, H.; Liebig, A.; Hjörvarsson, B.; Oppeneer, P. M.; Rubino, S.; Eriksson, O.; Leifer, K. Quantitative magnetic measurements with transmission electron microscope. *J. Magn. Magn. Mater.* **2010**, *322*, 1478–1480.
[52] Hu, Q. W.; Zhuo, Y.; Fu, X. X.; Zeng, Z. X.; Tang, P.; Zheng, C. L.; Huang, X. X. Assessing the achievable quantification accuracy of magnetic moments in noisy electron magnetic chiral dichroism spectra using modeling. *Appl. Phys. Lett.* **2025**, *126*, 102401.
[53] Ahlawat, A.; Khan, A. A.; Deshmukh, P.; Shirolkar, M. M.; Sinha, A. K.; Satapathy, S.; Sathe, V. G.; Choudhary, R. J. Correlation between spin-phonon coupling and magneto-electric effects in $CoFe_2O_4$/PMN-PT nanocomposite: Raman spectroscopy and XMCD study. *J. Mater. Sci.: Mater. Electron.* **2022**, *33*, 19766–19778.
[54] Valvidares, M.; Dix, N.; Isasa, M.; Ollefs, K.; Wilhelm, F.; Rogalev, A.; Sánchez, F.; Pellegrin, E.; Bedoya-Pinto, A.; Gargiani, P. et al. Absence of magnetic proximity effects in magnetoresistive Pt/$CoFe_2O_4$ hybrid interfaces. *Phys. Rev. B* **2016**, *93*, 214415.
[55] Löffler, S.; Schattschneider, P. A software package for the simulation of energy-loss magnetic chiral dichroism. *Ultramicroscopy* **2010**, *110*, 831–835.